Applied Surface Science 735 (2026) 166624

Contents lists available at ScienceDirect

Applied Surface Science

journal homepage: www.elsevier.com/locate/apsusc

Full Length Article

# Laser post-processing as a surface engineering strategy for atmospheric plasma-sprayed thin-film all-solid-state battery components

Arman Hasani [a,*], Chinmayee Nayak [a], Gidla Vinay [a], Antti Salminen [a], Shrikant Joshi [b], Sneha Goel [c], Vasanth Gopal [b], Ermei Makila [d], Mathias Juan [e], Ashish Ganvir [a]

[a] Digital Manufacturing and Surface Engineering (DMS) Research Group, Department of Mechanical and Materials Engineering, Faculty of Technology, University of Turku, Finland
[b] Department of Engineering Science, University West, Sweden
[c] Advanced Materials for Nuclear Energy, VTT Technical Research Centre of Finland, Finland
[d] Department of Physics and Astronomy, Faculty of Sciences, University of Turku, Finland
[e] SeaTech Engineering School, University of Toulon, France

ARTICLE INFO

*Keywords:*
Atmospheric plasma spraying
Laser post-processing
All-solid-state battery
Surface roughness
LTO thin-film
LLZO thin-film

ABSTRACT

The present study investigates laser post-processing as a method to tailor the surface properties of atmospheric plasma-sprayed (APS) anodes, solid electrolytes (SEs), and their half-cell configurations for all-solid-state batteries (ASSBs). $Li_4Ti_5O_{12}$ (LTO) was used as the anode material, $Li_7La_3Zr_2O_{12}$ (LLZO) as the solid electrolyte, and aluminum as the substrate. APS was successfully employed to deposit single-layer LTO and LLZO thin films, as well as a double-layer LTO–LLZO half-cell configuration. XRD analysis showed that the as-sprayed LTO and LLZO coatings retained their characteristic crystalline phases without significant structural changes. Pulsed laser post-processing enabled effective surface smoothing of the plasma-sprayed ASSB components, while also inducing material remelting, partial ablation, and architecture-dependent effects. Single-layer and multilayer configurations responded differently due to variations in melting point, optical absorption, and heat flow pathways. Microstructural and elemental analyses using SEM/EDS and optical profilometry were conducted to evaluate the influence of laser surface modification. In addition, XPS confirmed that no changes in chemical state occurred between the as-sprayed and laser-processed LLZO coatings. Overall, this proof-of-concept study demonstrates the potential of laser post-processing to improve the surface quality of APS-sprayed ASSB components and provides useful insights for battery manufacturing and thermal spray communities.

## 1. Introduction

The rapid expansion of electrification across sectors such as portable electronics, electric vehicles, and renewable energy storage has made efficient, high-performance batteries indispensable; energy storage systems are required to buffer intermittent renewable generation, support peak loads, and reduce reliance on fossil fuels while enabling seamless mobility and grid reliability [1]. Conventional lithium-ion batteries (LIBs) have dominated this landscape due to their high energy density, long cycle life, and scalability, powering everything from smartphones to EVs; however, they still face intrinsic limitations such as safety risks from flammable liquid electrolytes and theoretical energy density ceilings [2]. Consequently, all-solid-state batteries (ASSBs) have emerged as a promising next-generation technology featuring solid electrolytes that can potentially deliver higher energy density, improved safety, and longer lifespan by eliminating volatile liquids and enabling lithium-metal anodes, addressing key challenges of LIBs. Within ASSBs, thin-film all-solid-state batteries (TFASSBs) represent a specialized class where electrodes and electrolytes are deposited as dense and thin layers, offering enhanced interfacial contact, faster charge/discharge rates, lower self-discharge, and suitability for miniaturized and integrated applications, particularly in microelectronics and advanced portable systems. According to recent literature, these developments position TFASSBs as a critical frontier in solid-state battery research, though challenges such as interfacial stability, energy density optimization, and manufacturing scalability remain active areas of investigation [3–6]. However, studies show that interfacial degradation at the electrode-solid electrolyte interface in thin-film all-solid-state batteries can lead

* Corresponding author.
*E-mail address:* arman.hasani@utu.fi (A. Hasani).

https://doi.org/10.1016/j.apsusc.2026.166624
Received 22 January 2026; Received in revised form 12 March 2026; Accepted 15 March 2026
Available online 19 March 2026

to structural disorder, interphase formation, and capacity fading. In contrast, optimized thin-film battery architectures and improved material design strategies have demonstrated enhanced cycling stability, compatibility with low-temperature fabrication processes, and reliable operation over a wide temperature range for integratable microbattery applications [7,8].

In research on TFASSBs, a variety of thin-film deposition techniques have been explored to build dense, uniform electrode and electrolyte layers with controlled thickness and interfaces; conventional methods include vacuum-based physical and chemical techniques such as pulsed laser deposition (PLD), sputtering, atomic layer deposition (ALD), chemical vapor deposition (CVD), and sol–gel or spray pyrolysis approaches, which can produce high-quality thin films but are often slow, costly, and limited in scalability [9,10]. Within this landscape, thermal spray methods have recently gained attention as an emergent route for fabricating TFASSB components due to their high deposition rates, flexibility, and potential for scaled manufacturing compared with traditional vacuum-based, in-chamber processes [11,12]. One of the key thermal spray approaches used is suspension plasma spray (SPS), where finely suspended ceramic particles are injected into a plasma plume to form coatings; this has been applied to deposit $Li_4Ti_5O_{12}$ (LTO) thin-film electrodes and garnet solid electrolytes such as LLZO/LLZTO, demonstrating promising phase formation and microstructures suitable for ASSB use [13,14]. Atmospheric plasma spray (APS) has also been demonstrated as a pathway to fabricate individual anode (LTO), electrolyte (LLZO), and cathode (e.g., NMC) layers for solid-state battery architectures, though careful process optimization is needed to maintain phase integrity [11–16]. TFASSBs electrodes can be made in a single step using thermal spray techniques such as APS, SPS, low pressure plasma spraying (LPPS), and high velocity oxy-fuel (HVOF) spraying. Apart from overcoming the size, form, and multi-step fabrication process restrictions normally associated with conventional technologies, this integrated approach can also significantly boost production rates. Moreover, robotic deposition of ASSBs with intricate geometries is enabled by the application of thermal spray techniques [11,12,14–16].

Despite its scalability advantages, thermal spray processing introduces inherent limitations in thin-film batteries, particularly high surface roughness and non-homogeneous, and occasionally pore-infested interfaces caused by splat-based deposition and rapid solidification. These features hinder the formation of uniform electrode–electrolyte contact, leading to increased interfacial resistance and non-uniform current distribution. In TFASSBs, where performance is strongly interface-dominated, such imperfections can reduce ionic transport efficiency, rate capability, and cycling stability, while also promoting mechanical degradation such as cracking or delamination. As a result, mitigating surface roughness and interface heterogeneity is essential for realizing high-performance thermally sprayed thin-film batteries [17–19].

To mitigate surface roughness, porosity, and interface non-uniformity related issues inherent to thermally sprayed coatings, prior work has explored a range of post-processing and hybrid strategies originally developed for coatings in diverse applications (e.g., wear, corrosion, and thermal barriers) and more recently applied to battery materials. Several conventional strategies have been explored to modify and smooth the surface of ceramic solid electrolytes and battery electrodes prior to cell integration. Mechanical polishing is commonly employed to physically remove surface contamination layers and reduce roughness, thereby improving interfacial contact and lowering interfacial resistance in garnet-type electrolytes such as LLZO. For example, polishing treatments using abrasive papers or high-speed mechanical polishing have been shown to significantly reduce Li/LLZO interfacial resistance by improving surface flatness and contact area [20]. Chemical surface treatments, including wet chemical etching or chemical cleaning, have also been widely investigated to remove $Li_2CO_3$ and LiOH layers that form upon exposure of LLZO to air, thereby restoring the electrochemically active surface and improving Li wettability [21]. In addition, thermal annealing or heat treatment has been used to modify surface chemistry and microstructure, where high-temperature treatment can reduce surface carbonate contamination and improve interfacial electrochemical performance, although excessive heating may also lead to lithium loss or secondary phase formation. While these conventional approaches can improve surface quality and interfacial properties, they often involve multiple processing steps or may introduce mechanical damage or compositional changes. Consequently, alternative post-processing techniques such as laser surface treatment are being explored as rapid and localized approaches for surface modification of battery materials [22]. One widely studied approach is laser-based post-processing, which includes laser remelting, laser glazing, and localized thermal processing to reduce surface irregularities and seal open porosity in thermally sprayed deposits. In thermal spray surface engineering research, high-power lasers such as continuous-wave fiber lasers, $CO_2$ lasers, and Nd:YAG lasers have been used to melt and re-solidify the top layer of plasma, HVOF, or cold-sprayed coatings, resulting in denser, smoother microstructures with reduced porosity and improved mechanical properties compared to as-sprayed regions [23–25]. Laser surface texturing and laser remelting have also been shown to enhance adhesion, modify bond coat topography, and control microstructural features in thermal spray systems for non-battery applications [26,27]. Specifically for thermally sprayed battery materials, recent work on suspension plasma-sprayed (SPS) lithium titanate (LTO) electrodes demonstrated that fiber laser post-processing can significantly smoothen the uneven as-sprayed surface and alter morphology, which may translate into improved interfacial contact and reduced roughness in thin-films relevant to TFASSBs [14]. Parallel research on laser post-processing of SPS garnet-type LLZO solid-state electrolyte coatings has shown reduction in surface roughness (up to ~40%), accompanied by changes in phase constitution due to localized remelting, illustrating both the promise and complexity of laser interventions for improving surface quality and interface characteristics in thermally sprayed ASSB components [14,16]. Both continuous-wave fiber lasers and conventional $CO_2$/infrared lasers are used in thermal spray surface treatments. Continuous-wave lasers are mainly applied for remelting and surface smoothing, whereas longer-pulse or patterned laser approaches are explored for controlled texturing or adhesion in other coating applications. However, pulsed lasers are less commonly used for thermal spray post-processing than continuous-wave systems [27,28]. However, in the multi-layer architectures, the potential for laser energy to penetrate top layers and interact with underlying materials is a known challenge, often necessitating precise control over deposition and post-treatment parameters to maintain structural integrity. While recent advances have optimized thin-film cathodes using rapid thermal processing to mitigate side product formation and improve crystallinity, the specific examination of interdiffusion layers at electrode/electrolyte and electrode/substrate interfaces remains critical for ensuring stable electrochemical performance [29–31].

Based on available literature, significant research gaps remain in the systematic use of laser post-processing for enhancing attributes of thermally sprayed thin-film ASSB components. Although laser post-processing has been widely investigated for improving properties of thermal-sprayed coatings in non-battery applications, only limited studies address battery materials, and even fewer focus on solid-state or multilayer electrode–electrolyte architectures. In particular, the use of pulsed fiber lasers to mitigate surface roughness and interfacial inhomogeneity in thermally sprayed ASSB layers remains largely unexplored. Addressing these gaps, this work hypothesizes that pulsed fiber-laser post-processing can reduce surface roughness and improve interfacial homogeneity in thermally sprayed TFASSB components. To validate this, APS-deposited single-layer LTO and LLZO, as well as sequential double-layer LTO-LLZO thin-films, were fabricated as half-cell configuration on aluminum current collectors, and the effects of laser power, processing speed, pulse frequency, and hatch distance were systematically investigated with respect to microstructure, surface

roughness, and surface chemistry.

## 2. Materials and methods

### 2.1. Feedstock powders

Lithium Titanium Oxide ($Li_4Ti_5O_{12}$, LTO) powder (D50 = 6–7 μm, Toshima Manufacturing Co., Ltd., Japan) and Lithium Lanthanum Zirconium Oxide ($Li_7La_3Zr_2O_{12}$, LLZO) powder (D50 = 5–10 μm, Toshima Manufacturing Co., Ltd., Japan) were used as feedstock for coating deposition. Their chemical compositions, determined by EDS, are presented in Table 1. Morphologies of the as-received LTO and LLZO powders, shown in Fig. 1, were characterized by field-emission scanning electron microscopy (FE-SEM, Apreo S, Thermo Fisher Scientific, The Netherlands) equipped with EDS (UltimMax 100, Oxford Instruments, United Kingdom). LTO powder displayed angular particles with a narrow size distribution, while LLZO exhibited polyhedral shapes with a broader size range, consistent with supplier specifications.

The thin-films were deposited onto disk-shaped, commercial pure aluminum substrates (25 mm diameter, 2 mm thickness), which were grit blasted with a 125 μm alumina grit, and then cleaned prior to deposition.

### 2.2. Thin-film deposition

APS technique was used to fabricate the LTO anodes, LLZO electrolytes, and LTO-LLZO half-cells. A Mettech Axial III high-power plasma torch (Northwest Mettech Corp., Vancouver, Canada) equipped with a G4™ Gravimetric Powder Feeder was utilized for thin-film deposition. All spray parameters such as nozzle type, current, power, enthalpy, powder feed rate, and gas flow rate were selected based on preliminary trials published previously [11,12,15,16]. Aluminum discs of 25 mm diameter and 2 mm thickness served as substrates/current collectors. The experimental plan first comprised the deposition of single-layer LTO thin-films onto Al substrates mounted on a carousel using a fixture. Subsequently, during LLZO spraying, both bare Al substrates as well as prior single-layer LTO-deposited substrates were mounted on the carousel to generate single-layer LLZO thin-films as well as double-layer LTO-LLZO thin-films.

### 2.3. Laser post-processing

The entire surface of APS-sprayed single-layer LTO, single-layer LLZO and double-layer LTO-LLZO thin-films were post-processed using a pulsed fiber laser having a wavelength of 1070 ± 10 nm with a spot size of 400 μm. The present study explores the influence of key process parameters, such as laser power, scanning speed, frequency, and hatch distance, on the surface roughness of the as sprayed single-layer LTO, single-layer LLZO and double-layer LTO-LLZO thin-films. Based on several trials and previous studies [14,16] on laser post-processing of LTO, the laser processing parameters employed in this work, along with schematic representations of the corresponding laser post-processed regions, are presented in Tables 2–4 and Fig. 2. All regions designated with the A-label underwent laser post-processing over a 5 mm × 5 mm area to assess the influence of input variables on the single-layer LTO thin-film and establish optimal conditions for subsequent experiments. Then, as shown in Table 3, all regions designated with the B-label underwent laser post-processing over a 5 mm × 5 mm area to assess the influence of input variables on the single-layer LLZO thin-film and establish optimal conditions for subsequent experiments.

As summarized in Table 4, the laser post-processing parameters for the double-layer LTO-LLZO thin-films were selected based on the optimization results obtained from single-layer LTO and LLZO thin-films experiments. Among the tested parameter sets, region C-1 was chosen for detailed analysis because it consistently provided the most effective surface smoothing in the single-layer studies, while avoiding excessive melting or damage. For detailed analysis on sample C-1, the laser post-processing conditions were a scanning speed of 5 mm/s, a frequency of 100 kHz, a hatch spacing of 0.05 mm, and a laser power of 10 W for LTO-LLZO double-layers, as it exhibited the lowest Sa value. By optimizing these parameters, the surface roughness was significantly reduced, thereby enhancing the contact between the LTO anode and the LLZO solid electrolyte.

**Table 1**
Chemical composition of LTO and LLZO raw powders measured by EDS.

| | Li | Ti | O | La | Zr | C | Cl, Si, Al |
|---|---|---|---|---|---|---|---|
| LTO (raw powder) (wt %) | ND* | 54.4 | 45.2 | – | – | – | 0.4 |
| LLZO (raw powder) (wt %) | ND* | – | 25.1 | 46.0 | 18.1 | 10.7 | 0.1 |

(*Li is not detectable with Li is not detectable with windowed EDS).

### 2.4. Thin-film characterization

XRD analysis was carried out using a Bruker D8 twin-twin diffractometer (Bruker company, Germany). SEM observations were carried out with field-emission scanning electron microscopy (FE-SEM, Apreo S, Thermo Fisher Scientific, The Netherlands) equipped with EDS (UltimMax 100, Oxford Instruments, United Kingdom). SEM observations were conducted at an accelerating voltage of 5 kV, while EDS measurements were performed at 15 or 20 kV. For cross-section observation of as-sprayed samples a table-top SEM (Hitachi TM3000, Hitachi, Japan) in backscattered electron (BSE) mode was used. Surface topography and roughness of both laser-processed and as-sprayed regions were examined with an Alicona Infinite Focus G6 optical 3D measurement system (Bruker, Billerica, MA, USA) operated with MetMax software (ver. 3.0). Roughness values were reported in terms of the Sa parameter because Sa represents the arithmetic mean height over the measured region (not line), making it well suited for quantitative comparison of surface roughness between different processing conditions. Furthermore, the surface chemistry of the laser post-processed LTO, LLZO, and LTO-LLZO thin-films was investigated using an X-ray photoelectron spectrometer (XPS) (Nexsa, Thermo Fisher Scientific, United Kingdom).

## 3. Results

### 3.1. XRD analysis

To confirm the crystal structure and phase purity, XRD analysis was conducted on both LTO and LLZO powders along with the respective single-layer thin films. As shown in Fig. 3a, the XRD pattern of the single-layer LTO thin-film retains most of the characteristic peaks of the initial LTO powder before spraying. Nonetheless, a notable reduction in peak intensity is observed relative to the powder, likely due to morphological effects [11] such as particle flattening, surface roughness, and partial amorphization during deposition. These features reduce the number of well-oriented crystallites contributing to diffraction and increase diffuse scattering, leading to lower observed peak intensities. Another reason for the lower intensity peaks in the plasma sprayed single-layer LTO thin-film can be delithiation caused by lithium volatility at high temperatures [11,12]. Moreover, peak broadening suggests the presence of thermal stress in the thin-films caused by rapid quenching [32]. Apparently, the peak at approximately 25.3° corresponds to the anatase crystal structure of titanium dioxide. During plasma spraying of LTO, the anatase phase is often formed as an intermediate or residual phase due to complete Li loss and oxidation of $Ti^{3+}$ to $Ti^{4+}$ because of excessive high-temperature in plasma plume [15].

The XRD pattern of the single-layer LLZO thin film (Fig. 3b) exhibits most of the characteristic peaks corresponding to the LLZO feedstock

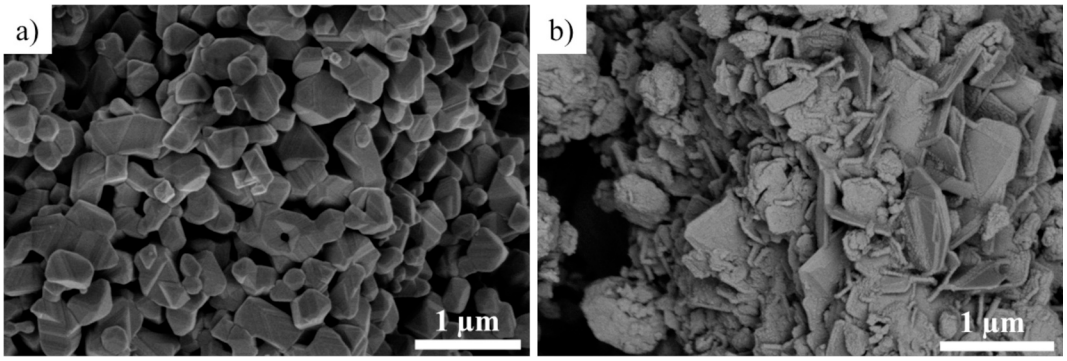


**Fig. 1.** SEM micrographs of the feedstock powders (a) LTO powder, (b) LLZO powder.

**Table 2**
Laser post-processing parameters for single-layer LTO thin-film regions.

| Region | Scanning speed (mm/s) | Frequency (kHz) | Laser power (W) | Hatch distance (mm) |
|---|---|---|---|---|
| A-1 | 5 | 100 | 5 | 0.05 |
| A-2 | 5 | 100 | 2.5 | 0.05 |
| A-3 | 2.5 | 100 | 5 | 0.05 |
| A-4 | 2.5 | 100 | 2.5 | 0.05 |
| A-5 | 5 | 25 | 5 | 0.05 |
| A-6 | 2.5 | 25 | 5 | 0.05 |
| A-7 | 5 | 100 | 5 | 0.075 |
| A-8 | 5 | 100 | 5 | 0.025 |

**Table 3**
Laser post-processing parameters for single-layer LLZO thin-film regions.

| Region | Scanning speed (mm/s) | Frequency (kHz) | Laser power (W) | Hatch distance (mm) |
|---|---|---|---|---|
| B-1 | 5 | 100 | 10 | 0.05 |
| B-2 | 5 | 100 | 7.5 | 0.05 |
| B-3 | 2.5 | 100 | 10 | 0.05 |
| B-4 | 2.5 | 100 | 15 | 0.05 |
| B-5 | 5 | 25 | 10 | 0.05 |
| B-6 | 2.5 | 25 | 15 | 0.05 |
| B-7 | 5 | 100 | 10 | 0.075 |
| B-8 | 5 | 100 | 10 | 0.075 |

**Table 4**
Optimized laser post-processing conditions for double-layer LTO-LLZO region.

| Region | Scanning speed (mm/s) | Frequency (kHz) | Laser power (W) | Hatch distance (mm) |
|---|---|---|---|---|
| C-1 | 5 | 100 | 10 | 0.05 |

powder in the 25°–35° 2θ range. In addition to these peaks, secondary phases such as $La_2Zr_2O_7$ are detected, likely arising from lithium evaporation at elevated temperatures. Similar to the single-layer LTO thin film, the LLZO thin film shows suppressed peak intensities, which can be attributed to the same factors discussed for the LTO thin-films. Furthermore, slight peak shifts and broadening are observed, indicating deviations in lattice parameters and the presence of thermal stresses or reduced crystallite size, respectively, induced by rapid solidification during the deposition process.

However, XPS analysis and surface morphology observations did not reveal significant chemical-state degradation after laser treatment. Furthermore, our recent synchrotron-based XRD study on laser interaction with LLZO showed that single-line laser scanning can modify minor phase fractions without causing complete amorphization of the garnet structure [16].

### 3.2. Cross-sectional analysis of as-sprayed thin-films

The SEM cross section micrographs of the as-sprayed single-layer LTO and LLZO as well as double-layer LTO-LLZO thin-films can be seen in Fig. 4a–c respectively. The microstructures presented here serve as a reference baseline; the corresponding laser post-processed microstructures are discussed in a subsequent section. The dense thin-film characteristic is crucial as it plays an important role in the fabrication of ASSB electrodes (with respective constituents), particularly in improving the pathways for Li-ion movement. The thickness of as-sprayed LTO and LLZO single-layer thin-films was found to be approximately 40 µm (Fig. 4d) and 30 µm (Fig. 4e), respectively, whereas in the double-layer LTO-LLZO thin-film the overall thickness was approximately 40 µm, the individual thicknesses of the LTO and LLZO layers were 23 µm and 17 µm, respectively. The thickness of the solid electrolyte should be lower to enhance the transport of Li ions [33,34]. For example, employing a 30 µm-thick LGPS ($Li_{9.54}Si_{1.74}P_{1.44}S_{11.7}Cl_{0.3}$) electrolyte can significantly increase the energy density from 100 W h $L^{-1}$ to approximately 460 W h $kg^{-1}$ [33].

### 3.3. Roughness analysis

Surface roughness of the as-sprayed and laser post-processed samples was evaluated using optical profilometry to determine the effectiveness of laser remelting on the APS-deposited thin-films. The results for the single-layer LTO and LLZO, as well as double-layer LLZO-LTO thin-films are shown in Figs. 5-7 respectively, with the corresponding Sa values summarized in Table 5. The as-sprayed thin-films exhibit roughness values of 9.75 µm and 6.11 µm for single-layer LTO (Fig. 5a) and LLZO (Fig. 6a), respectively and 4.6 µm for the double-layer LTO-LLZO double-layer (Fig. 7a), reflecting the characteristic splat morphology, inter-splat boundaries, and unmelted particle clusters inherent to APS processing. After laser post-processing, distinct trends emerge depending on the combination of laser parameters applied. For the single-layer LTO thin film (Fig. 5, A-series), several laser parameter sets resulted in partial surface smoothing with only modest reductions in roughness. In contrast, other conditions, such as A-2 (Fig. 5c), led to an increase in surface roughness due to insufficient melting. This observation is supported by the fact that both A-1 (identified as the optimal condition) and A-2 (exhibiting the highest roughness, even higher than the as-sprayed state) were processed using relatively low laser powers (5 W for A-1 and 2.5 W for A-2), which limited effective melting of the surface. The most effective smoothing for the single-layer LTO thin-film was obtained for region A-1 (Fig. 5b), where the roughness decreased from 9.75 µm to 5.7 µm, corresponding to a ~41.5% reduction. Although regions A-1, A-7, and A-8 were laser post-processed using the same laser power, frequency, and scanning speed, their surface roughness differed significantly due solely to variations in hatch distance. A hatch distance of 0.05 mm (A-1) provided an optimal overlap between adjacent laser tracks, enabling uniform remelting and effective smoothening of

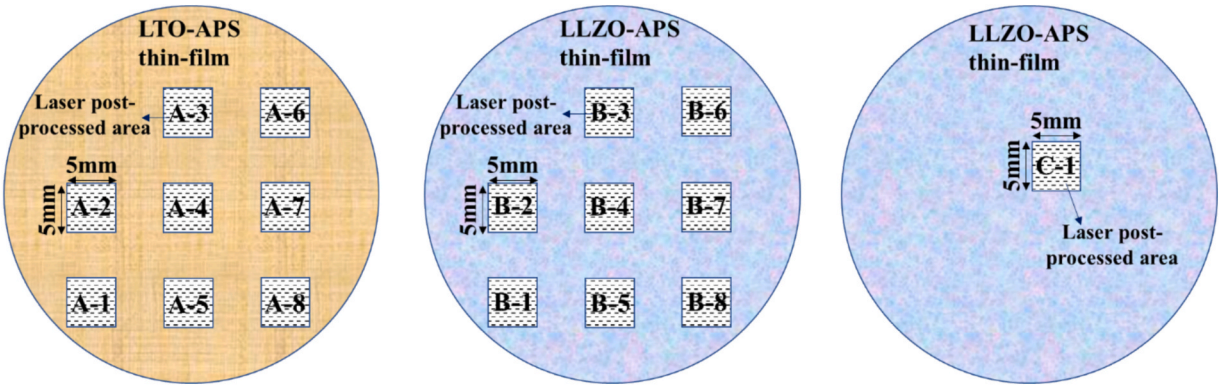


**Fig. 2.** Laser post-processing schematics for APS samples (a) A-1 to A-8, single-layer LTO, (b) B-1to B-8, single-layer LLZO-, and (c) C-1, double-layer LTO-LLZO corresponding to Tables 2, 3, and 4.

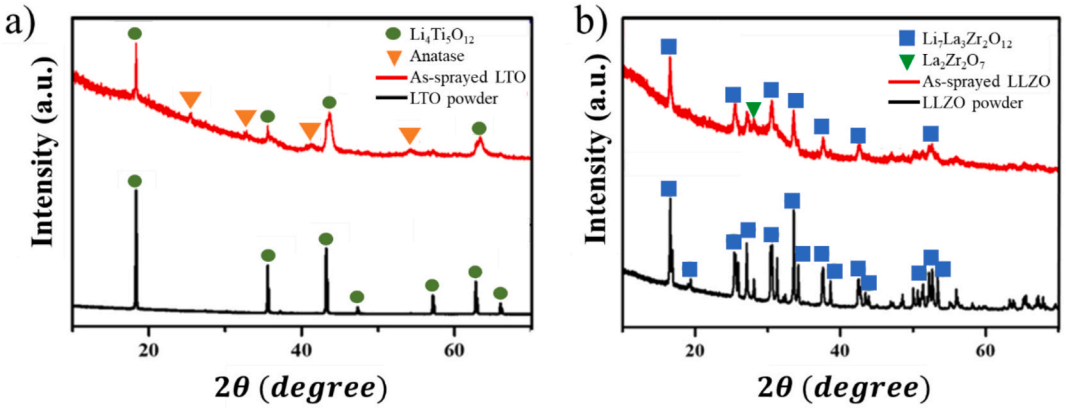


**Fig. 3.** XRD of Powders and single-layer thin-films (a) LTO, (b) LLZO.

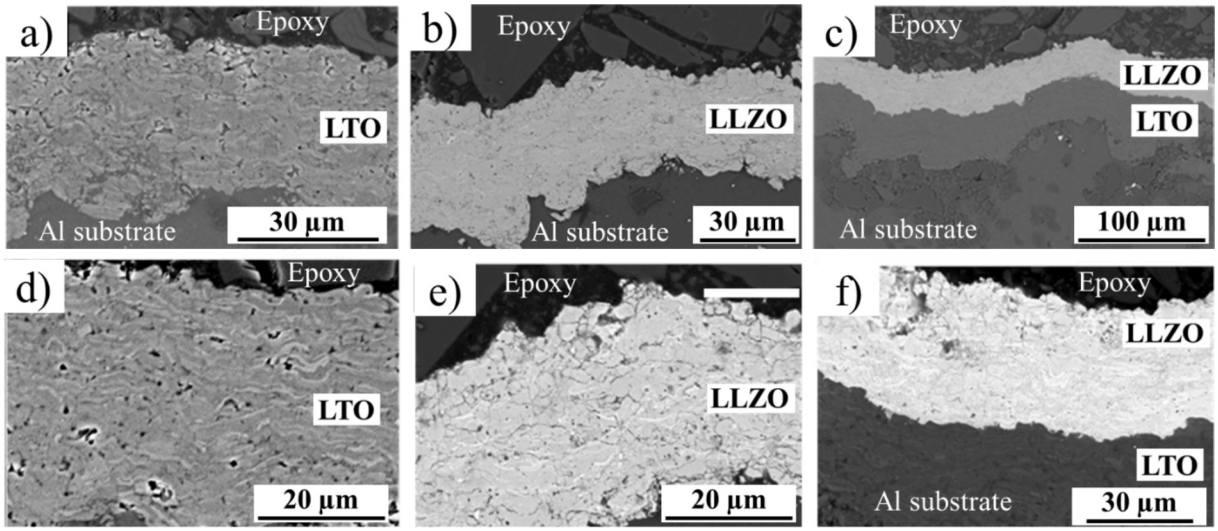


**Fig. 4.** SEM cross-section of thin-films (a) LTO, (b) LLZO, (c) LLZO on LTO and their magnified images in (d, e, and f), respectively.

asperities. In contrast, a larger hatch distance (A-7) resulted in insufficient overlap and incomplete smoothing of asperities, while a smaller hatch distance (A-8) led to excessive remelting and melt pool instability, causing partial re-roughening.

A similar behavior was observed for the single-layer LLZO thin-film (Fig. 6: B-series). The as-sprayed single-layer LLZO thin-film surface showed pronounced asperities that responded variably to different laser settings. For instance, region B-2 (Fig. 6c), B-5 (Fig. 6f), and B-6 (Fig. 6g) exhibited higher roughness values than the as-sprayed region, indicating unstable remelting or incomplete smoothening of surface peaks. In contrast, the optimized single-layer LLZO thin-film region, B-1 (Fig. 6b), achieved a significant reduction in roughness to 4.2 µm, representing an improvement of ~31.2%. The LTO-LLZO double-layer thin-film (Fig. 7: C-series) demonstrated the most pronounced smoothing effect, with the

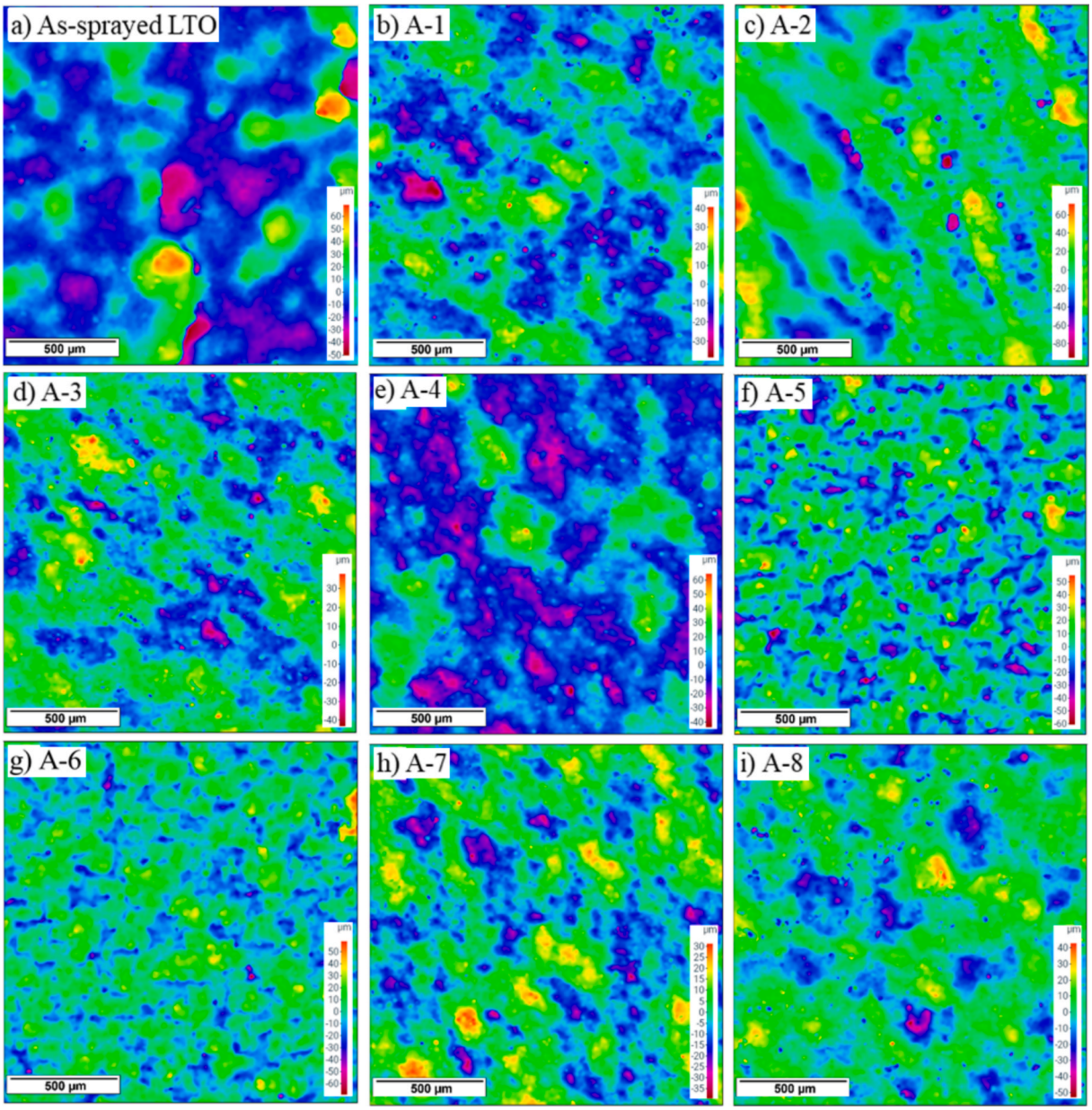


**Fig. 5.** Surface topography maps of single-layer LTO thin-film: As-sprayed (a) and laser-processed regions A-1 to A-8 (b–i) obtained by optical profilometry. Laser post-processing produces varying degrees of smoothing or roughening depending on parameter combinations. Region A-1 (b) shows the most significant reduction in surface roughness from 9.75 µm to 5.7 µm.

optimized parameter set (5 mm/s scanning speed, 100 kHz frequency, 10 W laser power, and 0.05 mm hatch spacing) reducing the roughness from 4.6 µm (Fig. 7a) to 2.75 µm (Fig. 7b), a ~40.2% improvement. This superior response may be attributed to the combined thermal and absorptive behavior of the LLZO top layer supported by the LTO underlayer in the double-layer thin-film architecture. Although the LLZO layer constitutes the laser-irradiated surface in the double-layer architecture, its response cannot be assumed to be identical to that of a single-layer LLZO thin-film. Due to the splat-based microstructure of APS-deposited LLZO, a fraction of the laser input energy penetrates through the top layer and is absorbed by the underlying LTO. As a result, the LTO underlayer acts as a secondary heat source and thermal buffer, prolonging the lifetime of the LLZO melt pool and promoting surface smoothening. This coupled thermal–optical interaction leads to more effective smoothing in the double-layer thin-film compared to the single-layer LLZO case, where heat is rapidly dissipated into the metallic substrate.

Across all three material systems, the general trend indicated that higher laser frequencies (particularly 100 kHz), moderate scanning speeds, and smaller hatch distances yielded more uniform melting and a more effective smoothening of asperities. The influence of laser power was also evident, while increased power enhanced smoothing by promoting the melt pool, excessive power occasionally intensified ablation or produced new surface irregularities, thereby increasing Sa. The combined analysis of Figs. 5–7 and Table 5 therefore highlights the strong parameter sensitivity of laser post-processing and underscores the importance of carefully balancing frequency, power, and scanning strategy to achieve optimal smoothing without introducing new defects.

### 3.4. Topography and elemental analysis

The surface topography of the as-sprayed single-layer LTO thin-film is shown in Fig. 8(a and b), where Fig. 8b is the magnified micrographs of Fig. 8a, highlighting the presence of mud cracks. Similarly, the surface

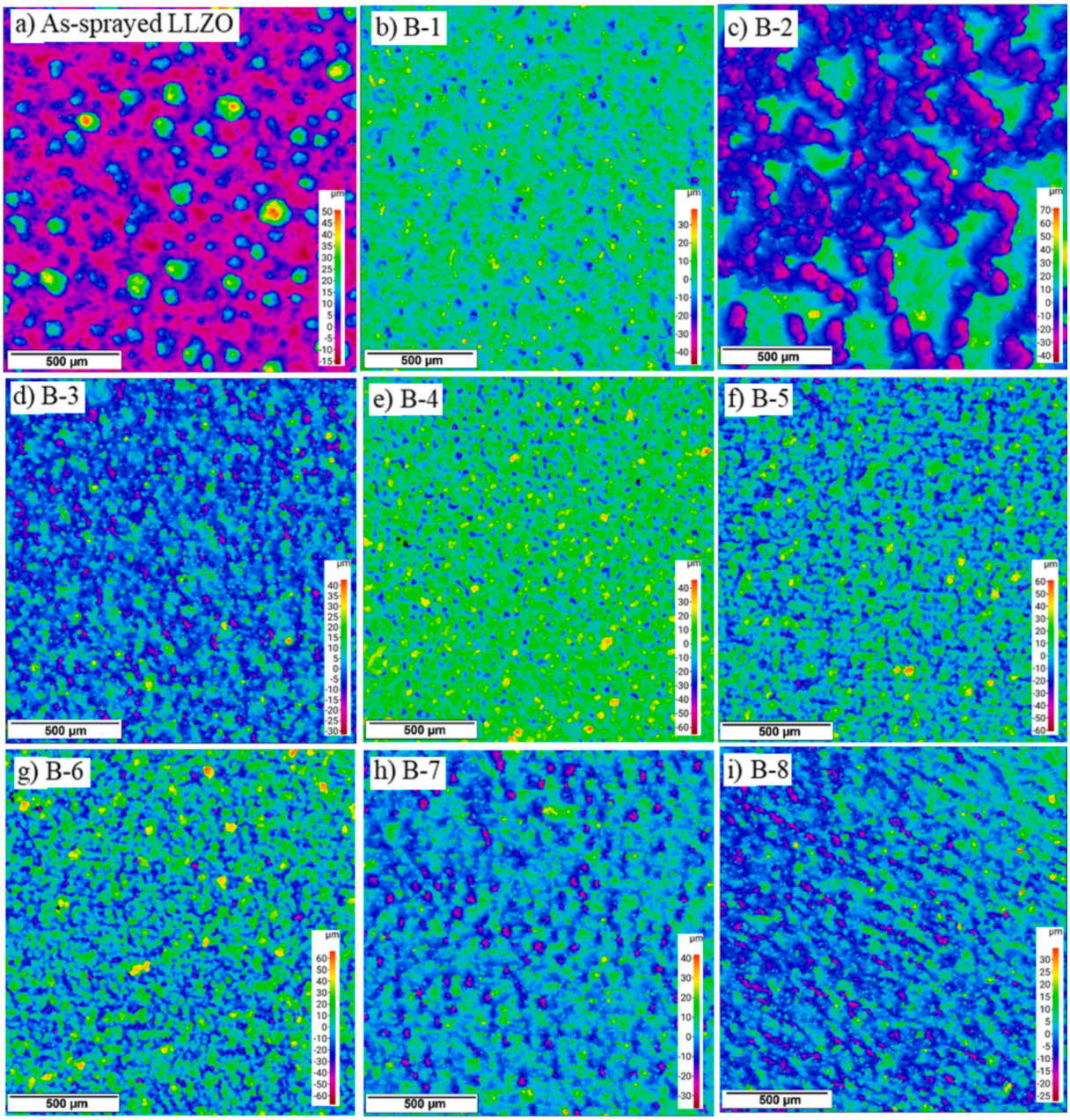


**Fig. 6.** Surface topography maps of single-layer LLZO thin-film: As-sprayed (a) and laser-processed regions B-1 to B-8 (b–i). LLZO exhibits stronger sensitivity to laser parameters; Region B-1 (b) provides the best smoothing, reaching a Sa of 4.2 µm.

morphology after laser post-processing of single-layer LTO thin-film (A-1) is presented in Fig. 8d and e, with Fig. 8e being enlarged views of Fig. 8d. These images confirm a smoother surface resulting from the laser post-processing. In the laser-post-processed regions, remelted zones and solidification cracks are clearly visible in Fig. 8b. Furthermore, EDS was performed to confirm the elemental composition of as-sprayed single-layer LTO thin-film (Fig. 8c) and laser post-processed single-layer LTO thin-film (Fig. 8f). EDS analysis confirms the presence of the main element Ti in LTO. As shown in Table 6, EDS quantitative analysis indicated that the concentrations of Ti and O remained essentially unchanged before and after laser post-processing. In contrast, the carbon content increased following laser post-processing, which can be attributed to surface reactions with ambient air and possible contamination during processing in ambient conditions.

The surface topography of the as-sprayed single-layer LLZO thin-film is shown in Fig. 9(a and b), where Fig. 9b is the magnified view of Fig. 9a, highlighting the presence of large peaks and valleys along with some mud cracks. Similarly, the surface morphology after laser post-processing of the as-sprayed single-layer LLZO thin-film is presented in Fig. 9d and e, with Fig. 9e being enlarged view of Fig. 9d. These images confirm a smoother surface resulting from the laser post-processing. In the laser post-processed region there are several spherical/semispherical particles with smooth surface which means complete melting has happened during laser post-processing, also there are some spots related to Al element which means due to laser post-processing in some regions the thin-film has been removed. However, similar laser post-processing approaches have also been successfully applied to thermally sprayed coatings deposited on low-melting substrates such as magnesium, demonstrating that careful control of laser parameters can enable coating modification without significant substrate melting [35]. Furthermore, EDS analysis was performed to confirm the elemental composition of as-sprayed single-layer LLZO thin-film (Fig. 9c) and laser

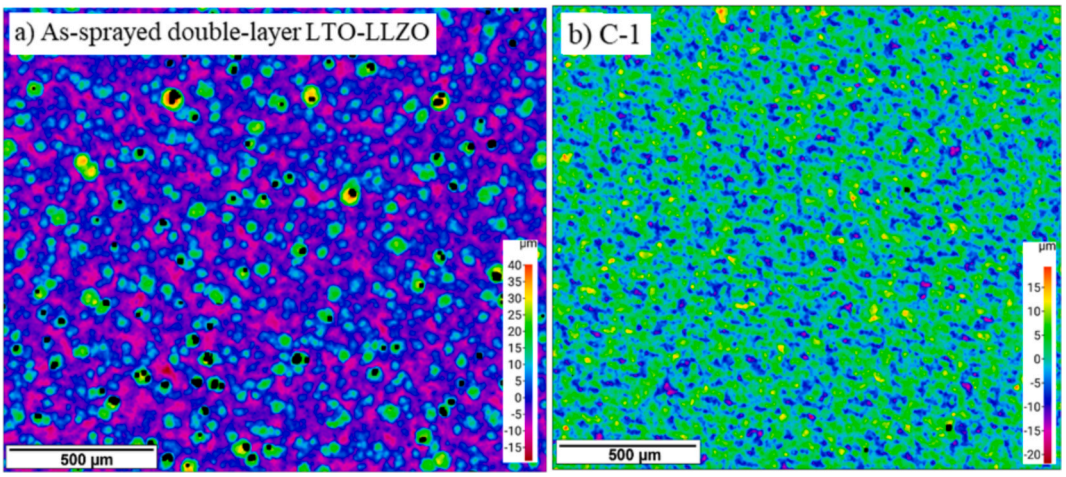


**Fig. 7.** Surface topography of double-layer LTO-LLZO thin-film: (a) As-sprayed double-layer; (b) Laser-processed C-1 region, where Sa for as sprayed and laser post-processed are 4.6 and 2.75 µm that shows approximately 40% decrease in surface roughness.

**Table 5**
Surface roughness comparison of laser post-processed regions along with the as-sprayed region.

| **Region** | **A-1** | **A-2** | **A-3** | **A-4** | **A-5** | **A-6** | **A-7** | **A-8** | **A-as-sprayed** |
|---|---|---|---|---|---|---|---|---|---|
| **Sa (µm)** | 5.7 | 11.56 | 6.12 | 6.68 | 9.35 | 7.93 | 6.17 | 5.96 | 9.75 |
| **Region** | **B-1** | **B-2** | **B-3** | **B-4** | **B-5** | **B-6** | **B-7** | **B-8** | **B-as-sprayed** |
| **Sa (µm)** | 4.2 | 9.2 | 5.12 | 7.37 | 9.17 | 11.34 | 4.85 | 4.3 | 6.11 |
| **Region** | **C-1** | | | | | | | | **C-as-sprayed** |
| **Sa (µm)** | 2.75 | | | | | | | | 4.6 |

post-processed single-layer LLZO thin-film (Fig. 9f). EDS results confirm the presence of the main element Zr and La in LLZO, while Li cannot be detected with windowed detector. It should be noted that lithium is difficult to quantify using EDS due to its low atomic number and weak X-ray emission. Therefore, although the overall elemental composition of Zr and La remains unchanged after laser processing, possible lithium redistribution or loss cannot be directly quantified using this technique. Previous studies on thin-film Li-based electrodes have shown that energetic processing routes such as sputtering, laser irradiation, or high-temperature treatments can induce lithium volatility or surface redistribution due to the high mobility and low boiling point of Li-containing species. Such effects have been discussed in recent thin-film electrode studies where compositional variations during energetic processing significantly influence electrochemical performance. Therefore, while the present work confirms that the primary cation framework of LLZO remains intact after laser post-processing, more quantitative techniques such as ICP-OES or SIMS would be required to directly evaluate lithium loss [36,37]. As shown in Table 7, EDS quantitative analysis shows that after laser post-processing, the oxygen atomic percentage increased from 33.4% to 44.3%, suggesting that laser irradiation promotes preferential oxidation of the LLZO thin-film. The oxygen enrichment observed by EDS can be attributed to laser-activated surface reactions involving lithium-containing species. In particular, lithium oxide present at the LLZO surface may undergo oxidation in ambient air ($Li_2O+½O_2 \rightarrow Li_2O_2$) during laser irradiation, followed by reaction with atmospheric $CO_2$ during cooling to form lithium carbonate ($Li_2O + CO_2 \rightarrow Li_2CO_3$) [22,38,39]. These reactions are expected to be confined to a thin near-surface region and produce poorly crystalline or amorphous species, which are below the detection limit of XRD but are consistent with the increased oxygen content measured by EDS and the carbonate-related features observed in XPS. Consequently, the relative atomic concentrations of other constituent elements, such as Zr and La, decreased due to the enhanced oxygen incorporation at the surface.

The surface topography of the as-sprayed double-layer LTO-LLZO thin-film is shown in Fig. 10a and b, where Fig. 10b is the magnified view of Fig. 10a, showcasing the smoother topography of the LLZO top layer than single-layer LLZO. Similarly, the surface morphology after laser post-processing of the as-sprayed LTO-LLZO double-layer thin-film is presented in Fig. 10d and e, with Fig. 10e being enlarged views of Fig. 10d. It is clear that the number of large bumpy particles on the surface of the as-sprayed thin-film significantly decreased after laser post-processing. In laser processed area, there are several spherical/semispherical particles with smooth surface indicating complete melting has happened during laser processing. In the laser post-processed regions, the presence of holes was observed, which can be attributed to localized laser beam penetration and subsequent re-melting that resulted in perforation of the thin-film. EDS scans were performed to confirm the elemental composition of as-sprayed LLZO thin-film (Fig. 10c) and LLZO laser post-processed thin-film (Fig. 10f). The presence of the main elements Zr and La in both as-sprayed and laser-processed double-layer LTO–LLZO thin films confirms that laser processing does not alter the overall elemental composition.

### 3.5. *Cross-sectional analysis of laser post-processed thin-films*

Cross-sectional microscopy analysis was performed to evaluate the penetration depth of the laser and its influence on thin-film integrity for all three configurations: single-layer LTO, single-layer LLZO, and double-layer LTO-LLZO. The representative optical micrographs are shown in Fig. 11. For the single-layer LTO thin-film, the as-sprayed microstructure (Fig. 11a) with a thickness of approximately ~40 µm. After laser post-processing (Fig. 11b), the thin-film thickness is reduced drastically indicating significant material removal. The transition region (Fig. 11c), where both the as-sprayed and laser post-processed zones are visible in a single cross section, clearly illustrates that the laser interaction resulted in ablation of the thin-film rather than selective

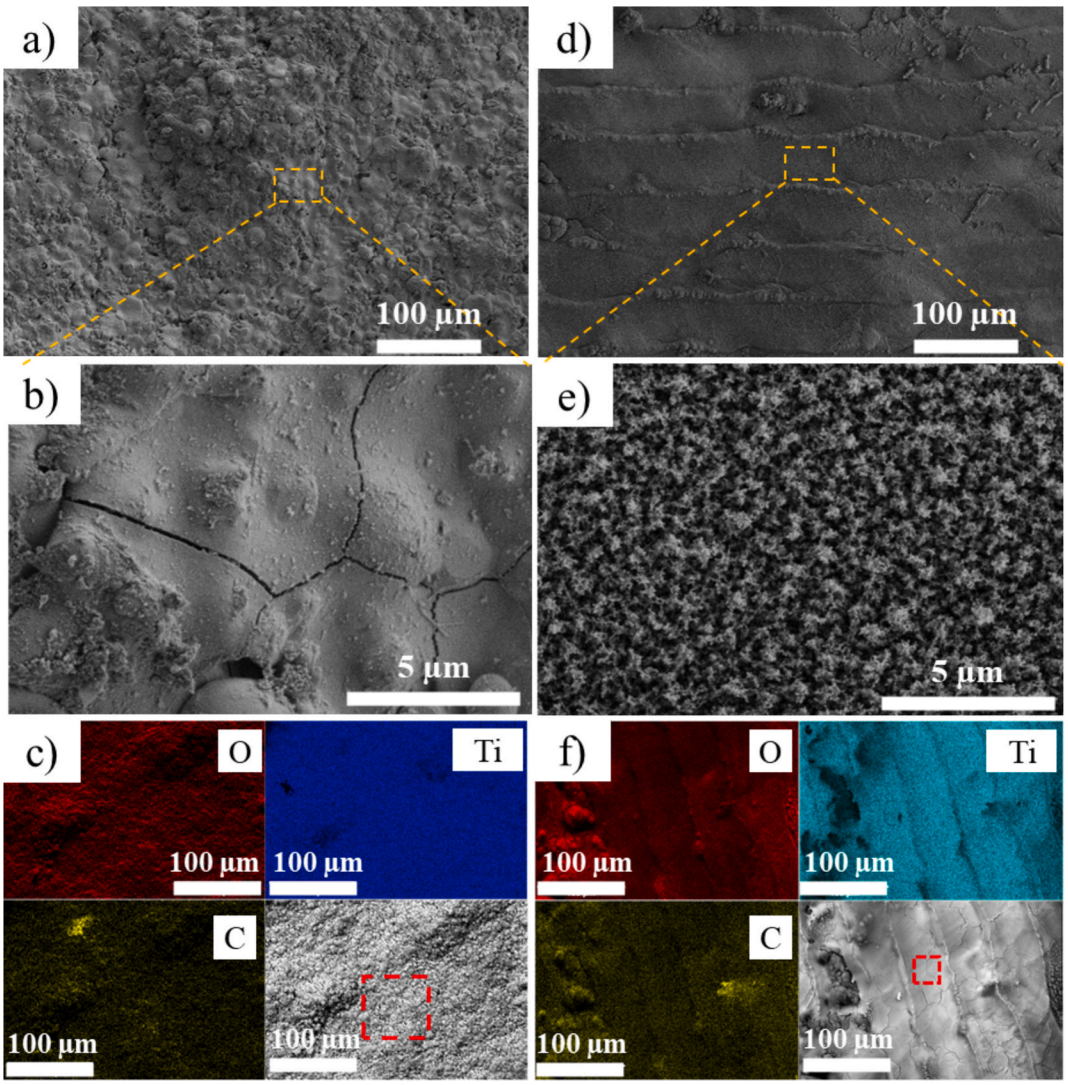


**Fig. 8.** SEM surface images and EDS elemental maps of the as-sprayed single-layer LTO thin-film (a, b, and c) and the laser post-processed region (A-1) (d, e, and f) show that microcracks are clearly visible at higher magnification in the as-sprayed thin-film (b), however, pronounced laser beam track features are evident on the surface of the laser post-processed region (d). Whereas these cracks are effectively eliminated after laser post-processing (e).

**Table 6**
Elemental composition of the red-highlighted spectrums in the single-layer LTO thin-film for the as-sprayed and laser post-processed samples.

| | Ti | O | C |
|---|---|---|---|
| As-sprayed region (obtained from selected spectrum) (wt %) | 51.9 | 44.1 | 4 |
| Laser post-processed region (obtained from selected spectrum) (wt %) | 42.3 | 51.2 | 6.5 |

remelting of only the asperity peaks. This confirms that for LTO, even relatively low laser power parameters can induce substantial thinning of the thin-film through rapid melting and expulsion of surface material. A similar trend is observed for the single-layer LLZO thin-film, shown in Fig. 11d–f. The as-sprayed LLZO thickness is approximately ~30 µm, but after laser processing, performed using higher power settings (as justified in section 2.3), the thickness decreases considerably. This again demonstrates that LLZO requires higher laser energy to initiate melting due to its thermal and optical properties, yet once melting occurs, material removal can be equally severe. The increased sensitivity to laser ablation compared to LTO is consistent with the LLZO surface observations where extensive spherical re-solidified particles were noted (see Fig. 9e).

The double-layer LTO-LLZO thin-film exhibits an even more complex response to laser processing. The optimized single-layer LLZO thin-film laser post-processing parameters were intentionally applied to the double-layer LTO-LLZO thin-film, as LLZO constitutes the top layer in this architecture. As shown in Fig. 11g–i, the laser not only ablated a significant portion of the LLZO thin-film but also interacted strongly with the underlying LTO thin-film. Surprisingly, the laser response differed substantially from the single-layer LLZO case: In the single-layer LLZO, the thin-film was thinned without affecting the substrate. In the double-layer LTO-LLZO, the same laser power resulted in melting of the LTO underlayer and partial intermixing with the aluminum substrate. To confirm this, EDS mapping was performed across the laser-interacted zone (Fig. 12). The elemental distribution clearly shows that the LTO thin-film was not removed, but instead re-melted and locally fused into the Al substrate, forming a metallurgically mixed interface. This demonstrates that under identical laser settings, the thermal transport and absorption behavior of a double-layer system is fundamentally different from that of a single ceramic thin-film. This behavior can be attributed to factors like surface roughness and material dependency of the laser.

Single-layer thin-film roughness depends primarily on the substrate roughness and number of spray passes. Double-layer roughness depends on the roughness of the LTO base thin-film, which was higher,

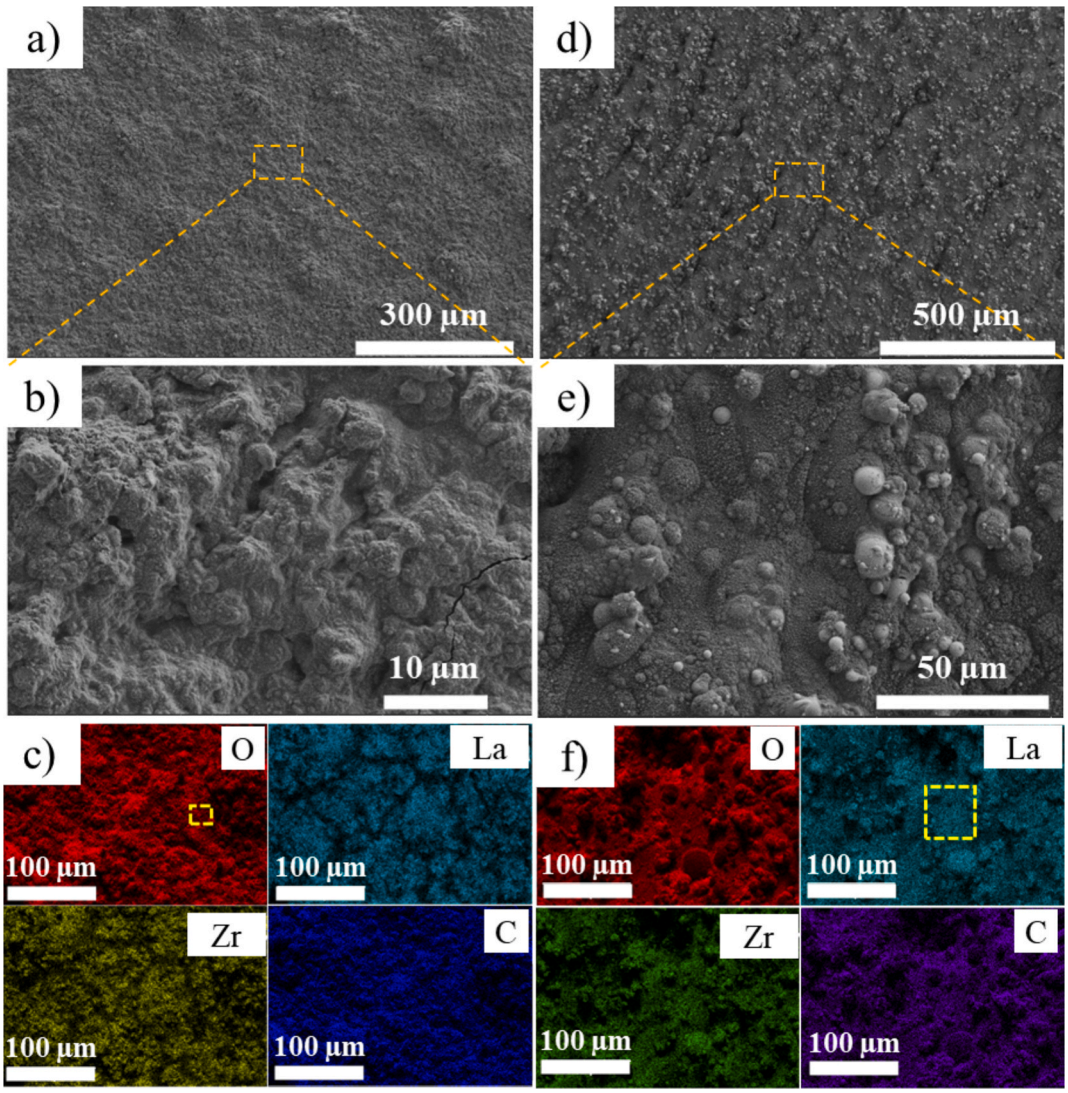


**Fig. 9.** SEM surface images and EDS elemental maps of the as-sprayed single-layer LLZO thin-film (a, b, and c) and the laser post-processed region (B-1) (d, e, and f) reveal that microcracks are clearly visible at higher magnification in the as-sprayed region (b), whereas these cracks are effectively eliminated after laser post-processing. In addition, pronounced laser beam track features are evident on the surface of the laser-processed region (d). Instead, many spherical, bumpy particles are formed following laser post-processing (e).

**Table 7**
Elemental composition of the yellow-highlighted spectrums in the single-layer LLZO thin-film for the as-sprayed and laser post-processed samples.

| | La | Zr | O | C | Al |
|---|---|---|---|---|---|
| As-sprayed region (obtained from selected spectrum) (wt %) | 39.8 | 12.9 | 33.4 | 13.9 | 0 |
| Laser post-processed region (obtained from selected spectrum) (wt %) | 28.2 | 10.4 | 44.3 | 14.5 | 2.6 |

promoting deeper and more uneven laser absorption into the double-layer LLZO thin-film. LTO exhibited strong interaction even at lower laser power. LLZO required higher power for melting, because the melting point of LLZO is approximately 1250 °C, whereas LTO melts or decomposes at a lower range of about 800–1000 °C [40–42].When these high LLZO parameters were used on the double-layer, the LTO thin-film absorbed a substantial portion of the laser energy, causing propagated remelting at the LTO-Al interface. Together, these results clearly demonstrate that laser interaction varies considerably depending on the chemistry, microstructure, and layering sequence of the plasma sprayed material system. The cross-sectional analysis is therefore essential in understanding how laser remelting should be tailored for: single-layer electrodes (LTO), single-layer solid electrolytes (LLZO), and multi-layer electrode–electrolyte stacks, such as LLZO-on-LTO.

### 3.6. Surface chemistry analysis

XPS was performed on the double-layer LTO-LLZO thin-film in both the as-sprayed (Fig. 13) and laser post-processed state (Fig. 14) to understand how laser post-processing influences the near-surface chemistry. The choice of this sample represents the actual half-cell configuration for a solid-state battery with solid electrolyte. The core-level spectra for C 1 s, O 1 s, Li 1 s, Zr 3d, La 3d and Ti 2p were examined for both conditions. The as-sprayed double-layer LTO-LLZO thin-film exhibits a surface that is heavily dominated by lithium-carbonate species, as evidenced by the strong carbonate-related contribution in the C 1 s region around ~289 eV (Fig. 13a) and the corresponding Li 1 s peak located at binding energies typical for $Li_2CO_3$ (Fig. 13b). This suggests that the LLZO surface undergoes significant carbonate formation during or immediately after the APS process, a behavior widely reported for garnet electrolytes exposed to high-temperature processing in ambient conditions [16,43,44]. A notable aspect of the as-sprayed

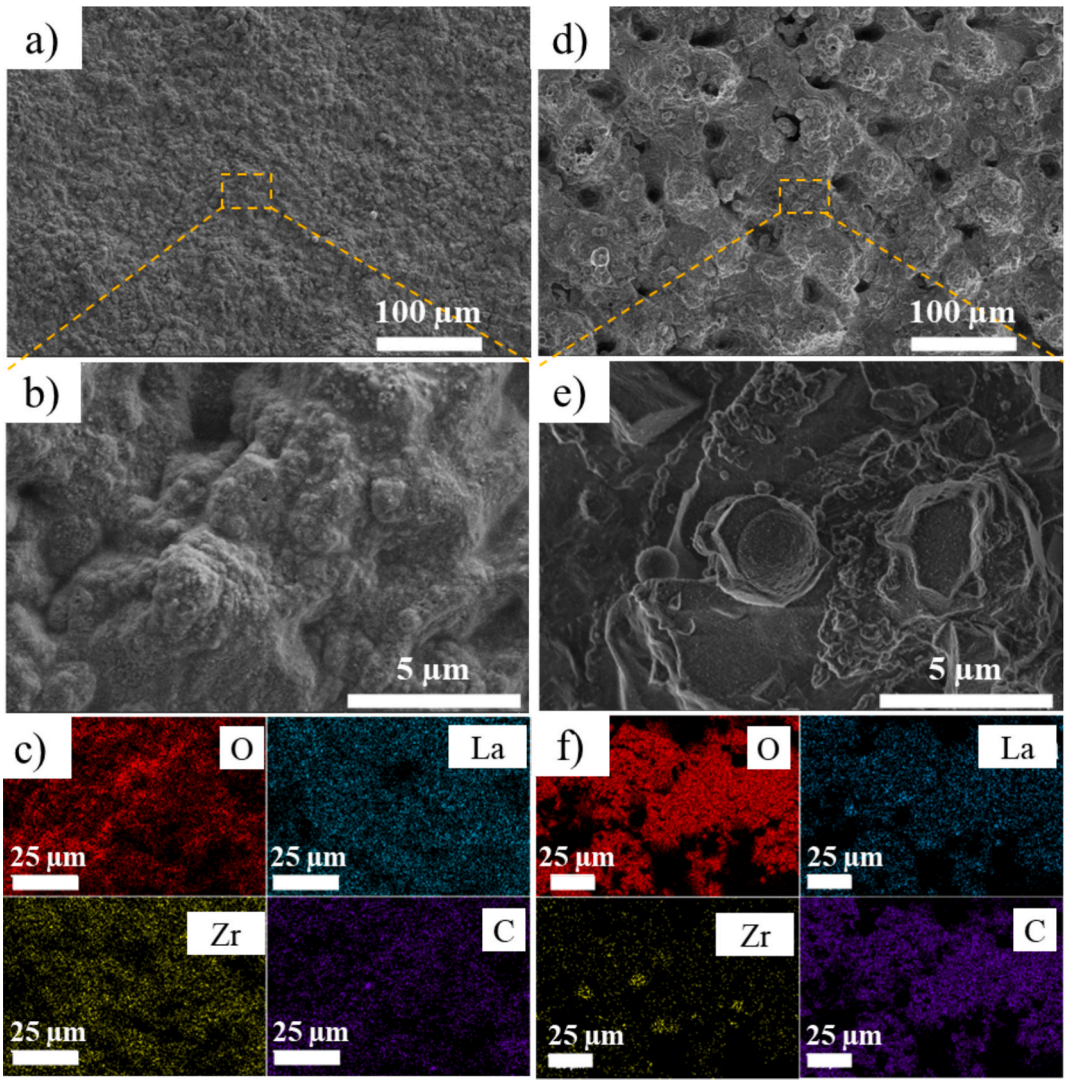


**Fig. 10.** SEM surface images and EDS elemental maps of as-sprayed double-layer LTO-LLZO thin-film (a, b, and c) and laser post-processed (d, e, and f) region (C-1). It is evident that there are several small holes on the surface due to pulsed laser interaction with LLZO layer.

XPS spectra is the absence of detectable Zr (Fig. 12c) and La (Fig. 13d) core-level signals. This can be attributed to the formation of a relatively thick Li-carbonate overlayer that exceeds the sampling depth of XPS, thereby masking the underlying garnet surface. Additionally, preferential lithium enrichment at the surface during APS driven by volatilization and rapid quenching may further suppress the detectable presence of heavier cations such as Zr and La. The core level Ti 2p is also collected and shown in Fig. 13f to confirm there is no Ti present in the LLZO top layer.

Following laser post-processing, the surface chemistry changes markedly, as evidenced by the XPS analysis (Fig. 14). Although the Li 1 s peak persists after laser post-processing (Fig. 14b), the relative intensity of carbonate species ($CO_3^{2+}$ in Fig. 14a) increases compared to the as-sprayed region. Importantly, the laser post-processed surface shows the reappearance of both Zr and La core-level signals (Fig. 14d and e), which were suppressed in the as-sprayed condition. The Zr 3d doublet, located at approximately 182.1 eV ($3d_5/_2$) and 184.5 eV ($3d_3/_2$), is consistent with the expected $Zr^{4+}$ oxidation state in LLZO. Similarly, the La 3d features appearing in the 834–839 eV range confirm the presence of $La^{3+}$ associated with the garnet lattice. The binding energies, peak shapes, and satellite features remain unchanged after laser post-processing, indicating that the oxidation states of Zr and La are preserved and that no detectable chemical degradation of the LLZO garnet framework occurs during laser post-processing. In contrast, Ti 2p peaks are detected in the laser post-processed sample (Fig. 14f), with Ti 2p3/2 and Ti 2p1/2 corresponding to Ti in the +4 oxidation state, characteristic of metal oxides. As observed from the EDS elemental maps (Fig. 12b and c), partial removal of the LLZO top layer occurs during laser post-processing, accompanied by localized remelting and redistribution of material from the underlying LTO layer. The presence of Ti in the XPS spectra therefore confirms the exposure and redistribution of the LTO layer following laser post-processing. Overall, the XPS results indicate that plasma spraying leads to surface carbonate contamination on LLZO, which partially obscures the intrinsic garnet chemistry. Laser post-processing effectively modifies the surface and enables the detection of underlying LLZO through the reappearance of La and Zr signals, while also revealing contributions from the underlying LTO thin-film due to partial remelting of both layers. Importantly, despite these morphological and compositional redistributions, the chemical states of all detected elements remain preserved relative to the as-sprayed condition, demonstrating that laser post-processing does not induce detrimental chemical changes in the coating system.

## 4. Discussion

The combined analysis of roughness evolution, surface morphology,

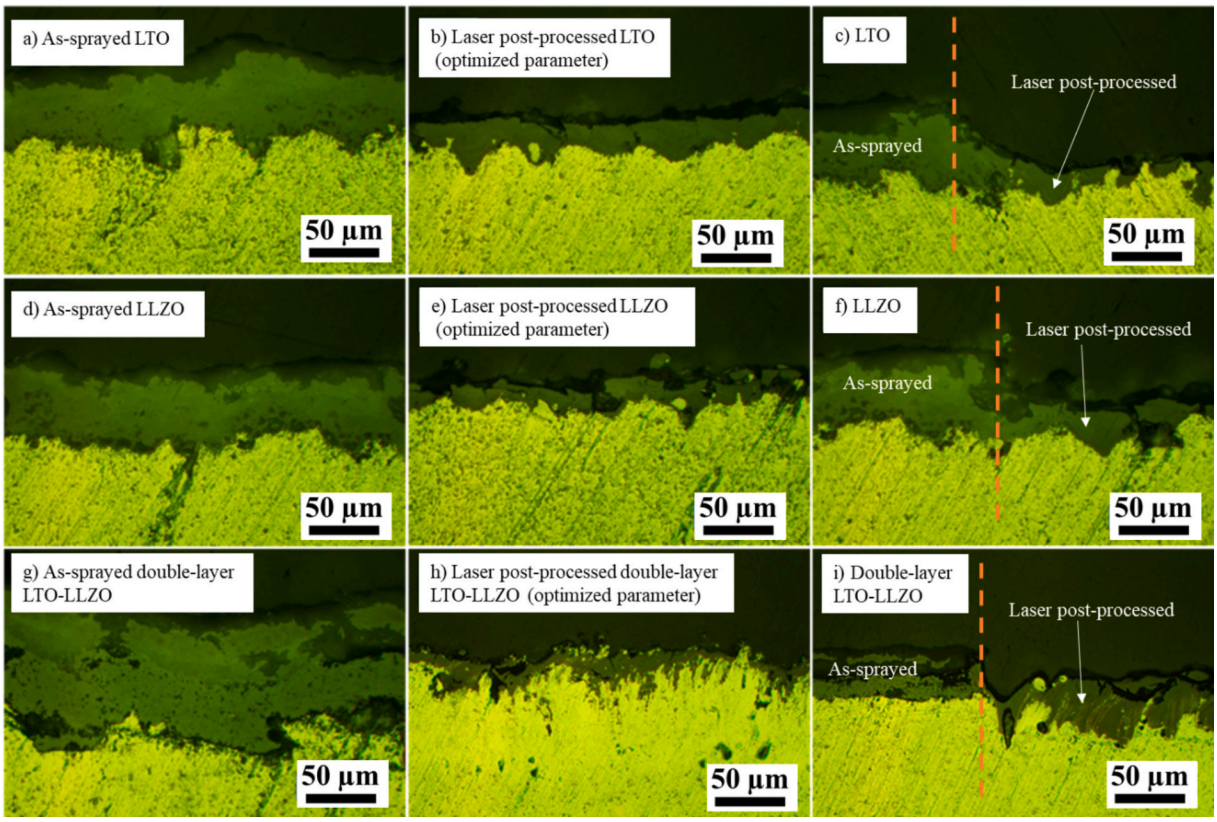


**Fig. 11.** Cross-section images of (a) As-sprayed LTO single-layer, (b) Laser post-processed LTO single-layer (optimized parameter), (c) comparing the transition from as-sprayed LTO single-layer to laser post-processed LTO single-layer region indicating the decrease of thickness, (d) As-sprayed LLZO single-layer, (e) Laser post-processed LLZO single-layer (optimized parameter), (f) comparing the transition from as-sprayed LLZO single-layer to laser post-processed LLZO single-layer region indicating the decrease of thickness, (g) As-sprayed LLZO on LTO double-layer, (h) Laser post-processed double-layer LTO-LLZO double-layer (optimized parameter), (i) comparing the transition from as-sprayed LTO-LLZO double-layer to laser post-processed LTO-LLZO double-layer region indicating the decrease of thickness.

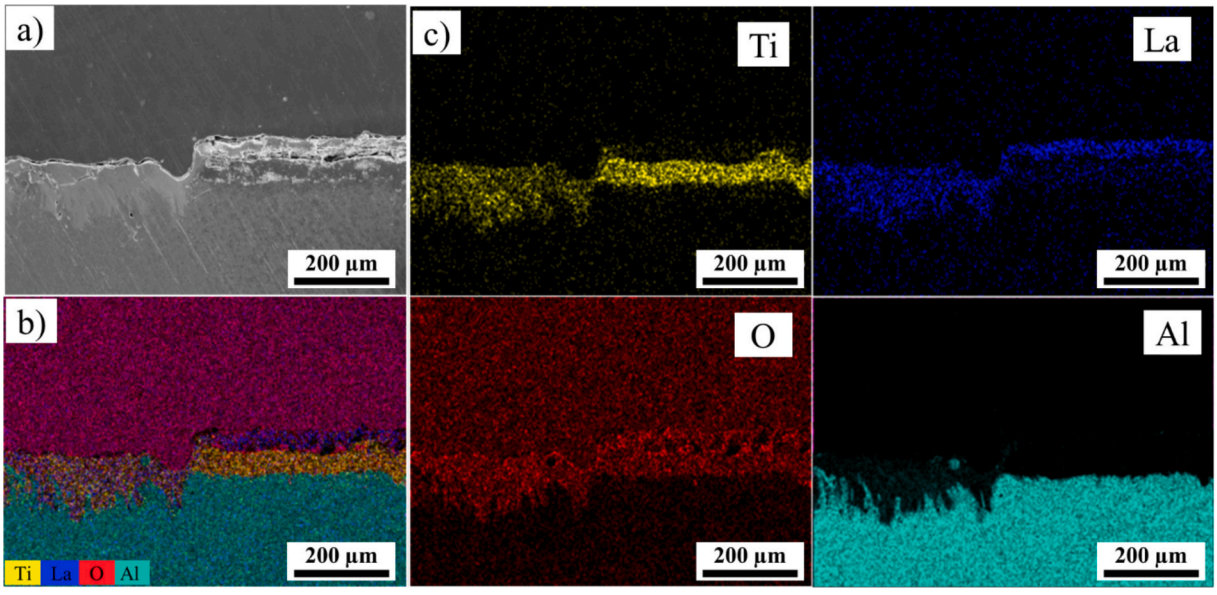


**Fig. 12.** Double-layer LTO-LLZO thin-film, (a) Cross-section SEM image showing the transition from the as-sprayed region to the laser-remelted region, highlighting the reduction in thin-film thickness; (b) EDS overlay map of all elements presents in the region shown in (a); and (c) individual elemental maps for Al, Ti, La, O, and C.

cross-sectional characteristics, and surface chemistry demonstrates that laser post-processing interacts with APS-deposited LTO and LLZO in a highly material and architecture-dependent manner. Although the aim of the laser post-processing was primarily to reduce the surface

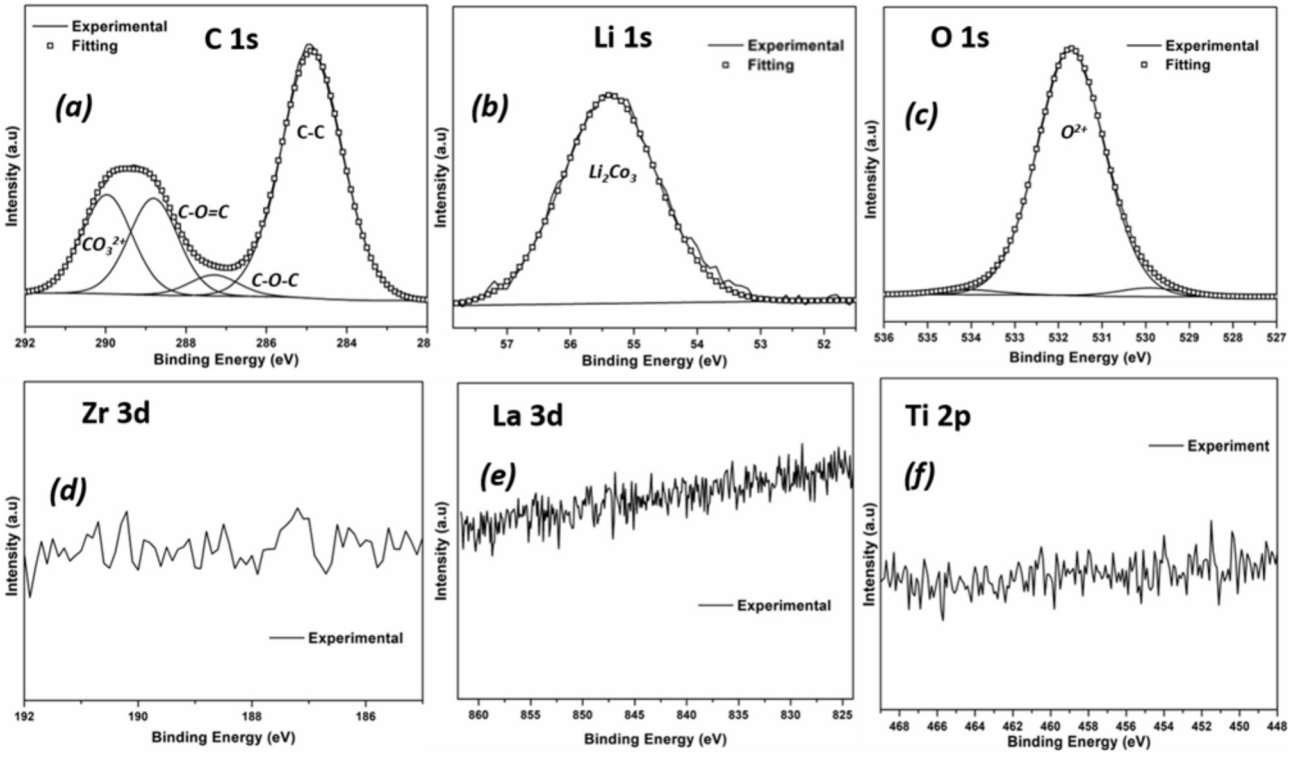


**Fig. 13.** XPS spectra of top LLZO layer showing the core level binding energy scans of C 1 s, Li 1s, O 1s Zr 3d, La 3d for APS double-layer LTO-LLZO (a, b, c, d, e) in as-sprayed condition (f) lack of detectable Ti 2p confirms titanium from the underlying LTO layer is not present.

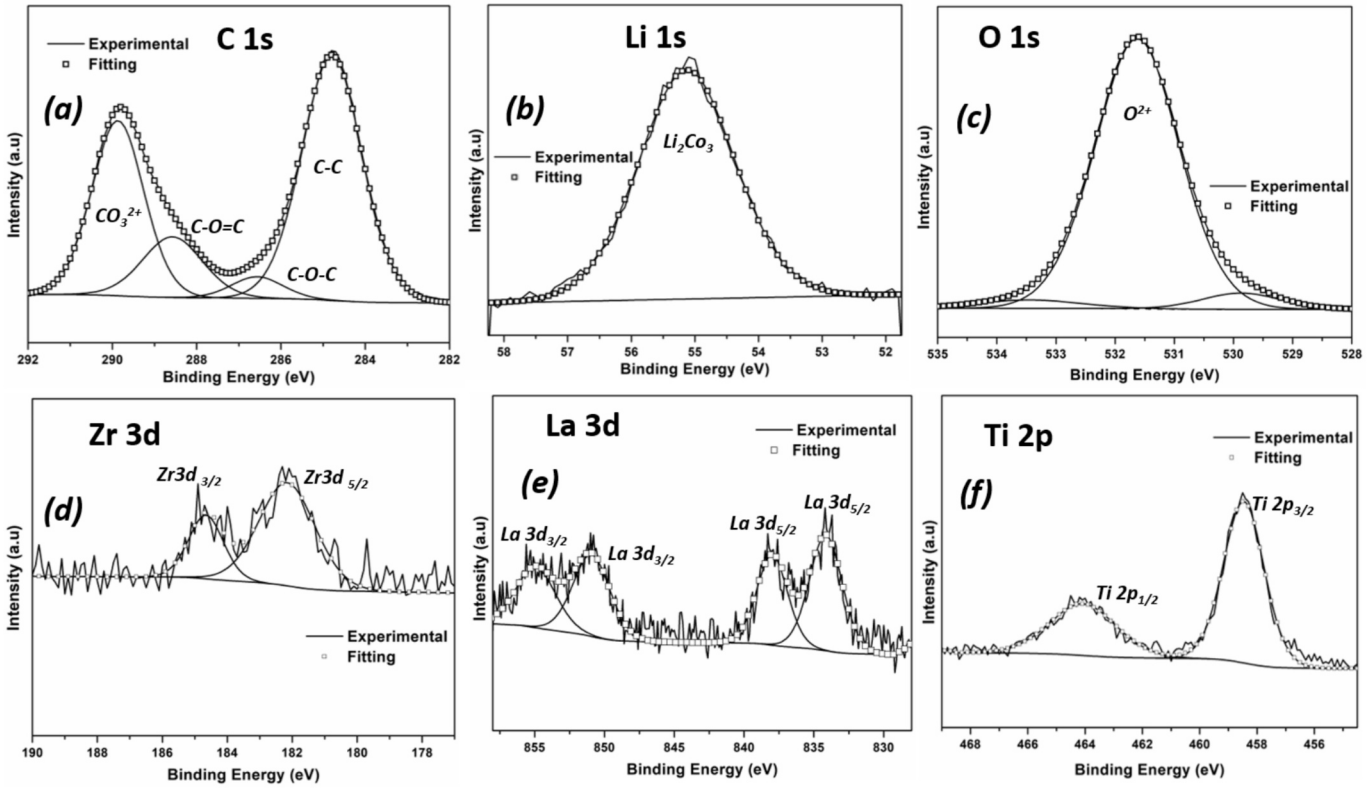


**Fig. 14.** XPS spectra of laser post processed APS double layer LLZO-LTO showing the core level binding energy scans of C 1s, Li 1s, O 1s Zr 3d, La 3d in (a, b, c, d, e) respectively, (f) Ti 2p is also shown for the same highlighting the presence of Ti from the beneath LTO layer.

roughness inherent to APS thin-films, the results clearly show that laser interaction extends far beyond simple smoothing. Instead, the laser induces a coupled response involving surface melting thereby remelting of splat boundaries and in many cases, significant material ablation.

These effects are governed by the intrinsic melting behavior, optical absorption characteristics, thermal conductivity, and microstructural heterogeneity of each layer, all of which dictate how the irradiated region stores and dissipates the incoming laser energy.

For LTO, which is comparatively more absorptive and has a lower melting point, the threshold between beneficial remelting and undesirable ablation is particularly narrow. Even moderate laser energy inputs resulted in the laser remelting effect which was visible clearly to the naked eye and also these energies chosen has resulted in thinning of the thin-film as well. On the other hand, LLZO, with its higher melting point and more refractory nature, requires higher laser energy to initiate melting; yet, once melting begins, LLZO forms rounded, spherical features after solidification. The same mechanism that enables smoothing also causes LLZO ablation, which explains the significant thickness loss observed in cross-sectional analysis. These effects become more pronounced in the double-layer LTO-LLZO configuration. Laser parameters optimized for single-layer LLZO induce predictable surface melting of the LLZO top layer, but the underlying LTO behaves differently. Because LTO absorbs laser energy more efficiently, the heat that penetrates through the LLZO thin-film leads to localized melting and partial mixing of LTO with the aluminum substrate. This result underscores a key insight: laser interaction in multilayer ceramic systems cannot be inferred directly from single-layer behavior. The thermal boundary conditions and heat flow pathways change fundamentally when a more absorptive material lies beneath a refractory layer, making thickness loss and deeper penetration more likely. These findings collectively highlight an important practical consideration for future implementations. If laser remelting is to be used as a post-processing technique for smoothing APS-sprayed electrodes or electrolytes, it may be necessary to deposit thin-films at higher initial thicknesses. This allows for a predetermined allowance for the inevitable material removal that accompanies laser-based smoothing, ensuring that the final functional thin-film remains sufficiently thick for electrochemical operation. In other words, laser remelting can be viewed not only as a surface smoothing strategy but also as an effective and controllable method for post-deposition thickness trimming. Such dual functionality could be strategically valuable for manufacturing routes where precise thickness control is desired after high-rate deposition processes like APS and other spray processes.

It is important to note that the present study utilized a pulsed laser with relatively low power, based on earlier single-line laser interaction studies performed by the same research group [14,16]. While these parameters were sufficient to demonstrate the feasibility of laser smoothing and to probe the material response, they represent only a small region of the broader processing window. Ongoing work in the group is now exploring continuous-wave (CW) lasers at higher power levels, which are expected to interact differently with these ceramic materials due to sustained thermal input rather than discrete pulses. Such investigations will help establish a more comprehensive understanding of the process envelope and enable more controlled smoothing or thickness modulation strategies suited for industrial-scale ASSB manufacturing. Overall, the findings of this study highlight that the interaction between laser energy and APS-sprayed ceramic battery materials is far more complex than simple surface remelting. These materials are highly sensitive to both smoothing and ablation, and the way heat flows through layered structures strongly influences the outcome. This underscores the need for carefully tailored laser parameters. In thin-film solid-state batteries, surface roughness plays a critical role in determining interfacial contact area and ionic transport pathways between the electrode and electrolyte layers. While surface roughness reduction is generally beneficial for improving interfacial contact in solid-state battery architectures, the present study also demonstrates that laser processing can introduce coating thinning and localized ablation. Therefore, optimization of coating thickness and laser parameters will be required before evaluating electrochemical performance of laser-treated electrodes. The insights gained here provide a foundation for optimizing laser-based post-processing strategies that achieve a balanced combination of surface smoothing, controlled thickness reduction, and structural integrity which are key requirements for next-generation thermal-sprayed ASSB components.

## 5. Conclusions

This study demonstrates the applicability of pulsed-laser post-processing as a tool to tailor surface roughness of APS thin-film components for ASSBs. The research successfully established that laser post-processing effectively reduces the surface roughness of APS-deposited LTO, LLZO, and LTO-LLZO thin-films when the processing parameters are properly optimized, achieving reduction of up to ~40% depending on the material system. The laser–material interaction leads to a combination of surface smoothing and ablation, with strongly material-dependent melting behavior: LTO melts readily and rapidly loses thickness, whereas LLZO requires higher energy input but undergoes deeper remelting followed by spherical re-solidification, and in double-layer systems the laser can penetrate the top layer and partially melt the underlying LTO. This surface smoothing is consistently accompanied by significant thinning of the coating thin-film, indicating that laser remelting inherently involves material removal. Consequently, practical applications may require higher initial coating thicknesses, and the process may also be exploited as a controlled method for post-processing thickness trimming. XPS analysis further reveals that as-sprayed LLZO surfaces are rich in carbonates that mask Zr and La signals, while laser post-processing effectively reduces this carbonate layer and exposes the underlying garnet chemistry without altering the oxidation states, demonstrating the chemical stability of LLZO during laser processing.

## CRediT authorship contribution statement

**Arman Hasani:** Writing – review & editing, Writing – original draft, Visualization, Validation, Software, Methodology, Investigation, Formal analysis, Data curation, Conceptualization. **Chinmayee Nayak:** Writing – review & editing, Writing – original draft, Validation, Supervision, Methodology, Investigation, Conceptualization. **Gidla Vinay:** Writing – review & editing, Writing – original draft, Visualization, Validation, Software, Methodology, Investigation, Formal analysis, Data curation, Conceptualization. **Antti Salminen:** Writing – review & editing, Supervision, Resources, Funding acquisition. **Shrikant Joshi:** Writing – review & editing, Project administration, Methodology. **Sneha Goel:** Writing – review & editing, Supervision. **Vasanth Gopal:** Writing – review & editing, Methodology, Investigation. **Ermei Makila:** Writing – review & editing, Investigation, Formal analysis. **Mathias Juan:** Writing – review & editing, Software, Methodology, Investigation, Formal analysis, Data curation, Conceptualization. **Ashish Ganvir:** Writing – review & editing, Supervision, Resources, Project administration, Funding acquisition, Conceptualization.

## Declaration of competing interest

The authors declare that they have no known competing financial interests or personal relationships that could have appeared to influence the work reported in this paper.

## Acknowledgments

The authors would like to acknowledge the invaluable contributions of Stefan Björklund from University West, Trollhättan, Sweden, for his assistance with plasma spraying of the battery materials, and Aki Piiroinen form University of Turku for his assistance with laser post-processing. The authors also acknowledge the Finnish Digital Design and Manufacturing Infrastructure (FiDiEm) for access to the experimental facilities. We acknowledge the Materials Research Infrastructure (MARI) at Department of Physics and Astronomy, University of Turku for access and support with the SEM, XPS and XRD facilities.

*Declaration of generative AI and AI-assisted technologies in the writing process*

During the preparation of this work the author(s) used [ChatGPT] in order to [English Language Proofreading]. After using this tool/service, the author(s) reviewed and edited the content as needed and take(s) full responsibility for the content of the published article.

*Funding*

The Authors acknowledges financial support from GREEN-BAT (352517), co-funded by the Research Council of Finland and the European Union under the M-ERA.NET 2021 framework, as well as the SOLACE (DNR 360540) Academy research fellowship, funded by the Research Council of Finland. Prof. Ashish Ganvir also extends his gratitude to the City of Turku for supporting his tenure-track grant. Prof. Antti Salminen acknowledges financial support through the DREAMS TENK TOT project (5159/31/2021), funded by Business Finland. The authors also acknowledge the Finnish Digital Design and Manufacturing Infrastructure (FiDiEm) for access to the experimental facilities. The Swedish portion of this research, conducted at University West, Sweden, was funded by the following projects: (a) the proof-of-concept project NovelCABs, supported by the Swedish Energy Agency (Energimyndigheten, Dnr 2021-002227), and (b) the transnational M-ERA.NET 3 project GREEN-BAT, with backing from the European Commission, with Vinnova (the Swedish Governmental Agency for Innovation Systems) as the national financier for Swedish participation. This project has received funding from the European Union's Horizon 2020 research and innovation program under grant agreement No 958174.

## Data availability

Data will be made available on request.

## References

[1] M.M. Hasan, et al., Advancing energy storage: the future trajectory of lithium-ion battery technologies, J. Energy Storage 120 (2025) 116511, https://doi.org/10.1016/j.est.2025.116511.
[2] N.C. Paranamana, A. Werbrouck, A.K. Datta, X. He, M.J. Young, Understanding cathode-electrolyte interphase formation in solid state Li-ion batteries via 4D-STEM, Adv. Energy Mater. 15 (2025) 11, https://doi.org/10.1002/aenm.202403904.
[3] S. Antony Jose, et al., Solid-state lithium batteries: advances, challenges, and future perspectives, Batteries 11 (3) (2025) 90, https://doi.org/10.3390/batteries11030090.
[4] C. Wu, et al., Current status and future directions of all-solid-state batteries with lithium metal anodes, sulfide electrolytes, and layered transition metal oxide cathodes, Nano Energy 87 (2021) 106081, https://doi.org/10.1016/j.nanoen.2021.106081.
[5] A. Machín, C. Morant, F. Márquez, Advancements and challenges in solid-state battery technology: an in-depth review of solid electrolytes and anode innovations, Batteries 10 (1) (2024) 29, https://doi.org/10.3390/batteries10010029.
[6] P.U. Nzereogu, et al., Solid-State lithium-ion battery electrolytes: Revolutionizing energy density and safety, Hybrid Adv. 8 (2025) 100339, https://doi.org/10.1016/j.hybadv.2024.100339.
[7] Q. Xia, et al., Integratable and Wide-temperature all-solid-state thin film lithium-ion microbatteries based on $Li_xMnO_2/Nb_2O_{5-x}$ configuration, Adv. Funct. Mater. 36 (2026) 9, https://doi.org/10.1002/adfm.202516265.
[8] Q. Xia, et al., Unraveling the $LiMn_2O_4$/LiPON interface degradation in all-solid-state thin-film lithium batteries, Nano Lett. 25 (19) (2025) 7892–7899, https://doi.org/10.1021/acs.nanolett.5c01315.
[9] B. Wu, C. Chen, D.L. Danilov, R.-A. Eichel, P.H.L. Notten, All-solid-state thin film Li-ion batteries: new challenges, new materials, and new designs, Batteries 9 (3) (2023) 186, https://doi.org/10.3390/batteries9030186.
[10] Y. Yu, M. Gong, C. Dong, X. Xu, Thin-film deposition techniques in surface and interface engineering of solid-state lithium batteries, Next Nanotechnol. 3–4 (2023) 100028, https://doi.org/10.1016/j.nxnano.2023.100028.
[11] V. Gopal, et al., Exploring atmospheric plasma spraying as a pathway to fabricate solid-state battery constituents, Surf. Coat. Technol. 502 (2025) 131945, https://doi.org/10.1016/j.surfcoat.2025.131945.
[12] S. Mathiyalagan, et al., Facile one-step fabrication of $Li_4Ti_5O_{12}$ coatings by suspension plasma spraying, Mater. Res. Bull. 181 (2025) 113111, https://doi.org/10.1016/j.materresbull.2024.113111.
[13] I. Koresh, Z. Tang, T. Troczynski, A novel approach to prepare Li-La-Zr-O solid state electrolyte films by suspension plasma spray, Solid State Ion. 368 (2021) 115679, https://doi.org/10.1016/j.ssi.2021.115679.
[14] A. Hasani, et al., Laser Processing of liquid feedstock plasma-sprayed lithium titanium oxide solid-state-battery electrode, Coatings 14 (2) (2024) 224, https://doi.org/10.3390/coatings14020224.
[15] A. Hasani, et al., Localized phase and elemental mapping in solid-state lithium battery LTO anode thin-film produced by a novel suspension plasma spray approach, J. Therm. Spray Technol. (2025), https://doi.org/10.1007/s11666-025-02003-6.
[16] A. Hasani, et al., Advanced synchrotron micro characterization of laser post-processed plasma sprayed LLZO solid-state battery electrolyte, IOP Conf. Ser.: Mater. Sci. Eng. 1332 (1) (2025) 012022, https://doi.org/10.1088/1757-899X/1332/1/012022.
[17] S. Slegers, M. Linzas, J. Drijkoningen, J. D'Haen, N. Reddy, W. Deferme, Surface roughness reduction of additive manufactured products by applying a functional coating using ultrasonic spray coating, Coatings 7 (12) (2017) 208, https://doi.org/10.3390/coatings7120208.
[18] A. Lanzutti, et al., The use of thin films as defect sealants to increase the corrosion resistance of thermal spray coatings, Metals (Basel) 13 (10) (2023) 1778, https://doi.org/10.3390/met13101778.
[19] B. Ransom, et al., Electrolyte coatings for high adhesion interfaces in solid-state batteries from first principles, ACS Appl. Mater. Interfaces 15 (37) (2023) 44394–44403, https://doi.org/10.1021/acsami.3c04452.
[20] X. Ma, Y. Xu, Effects of polishing treatments on the interface between garnet solid electrolyte and lithium metal, Electrochim. Acta 441 (2023) 141789, https://doi.org/10.1016/j.electacta.2022.141789.
[21] T. Ohnishi, I. Sakaguchi, K. Takada, Surface treatment of garnet-type solid electrolyte for suppressing dendritic growth, ACS Appl. Energy Mater. 7 (13) (2024) 5321–5325, https://doi.org/10.1021/acsaem.4c00805.
[22] H. Zhang, et al., On high-temperature thermal cleaning of $Li_7La_3Zr_2O_{12}$ solid-state electrolytes, ACS Appl. Energy Mater. 6 (13) (2023) 6972–6980, https://doi.org/10.1021/acsaem.3c00459.
[23] Z. Shengbin, J. Chenpeng, Y. Yuxue, W. Lixin, H. Yiming, Y. Lijun, Effects of laser remelting on microstructural characteristics of Ni-WC composite coatings produced by laser hot wire cladding, J. Alloys Compd. 908 (2022) 164612, https://doi.org/10.1016/j.jallcom.2022.164612.
[24] C.J. Múnez, J. Gómez-García, F. Sevillano, P. Poza, M.V. Utrilla, Improving thermal barrier coatings by laser remelting, J. Nanosci. Nanotechnol. 11 (10) (2011) 8724–8729, https://doi.org/10.1166/jnn.2011.3457.
[25] K. Yang, J. Li, Q. Wang, Z. Li, Y. Jiang, Y. Bao, Effect of laser remelting on microstructure and wear resistance of plasma sprayed $Al_2O_3$-40%$TiO_2$ coating, Wear 426–427 (2019) 314–318, https://doi.org/10.1016/j.wear.2019.01.100.
[26] M.S. Ahmadi, R. Shoja-Razavi, Z. Valefi, H. Jamali, The effect of laser surface treatment on the thermal shock behavior of plasma sprayed $Al_2O_3$/YSZ multilayer thermal barrier coatings, Surf. Coat. Technol. 366 (2019) 62–69, https://doi.org/10.1016/j.surfcoat.2019.03.024.
[27] R. Kromer, S. Costil, C. Verdy, S. Gojon, H. Liao, Laser surface texturing to enhance adhesion bond strength of spray coatings – cold spraying, wire-arc spraying, and atmospheric plasma spraying, Surf. Coat. Technol. 352 (2018) 642–653, https://doi.org/10.1016/j.surfcoat.2017.05.007.
[28] D. Shen, X. Zhang, L. Zhu, Laser processing for electricity generators: physics, methods and applications, Nano Energy 120 (2024) 109182, https://doi.org/10.1016/j.nanoen.2023.109182.
[29] S. Behera, S. Lee, I. Oda-Bayliss, C. Kumar Panda, S. Yagi, H.-S. Kim, Optimizing sodium ion battery performance with $V_2O_5$ thin film cathodes, Results Mater. 28 (2025) 100780, https://doi.org/10.1016/j.rinma.2025.100780.
[30] Q. Xia, et al., All-solid-state thin film lithium/lithium-ion microbatteries for powering the internet of things, Adv. Mater. 35 (2023) 2, https://doi.org/10.1002/adma.202200538.
[31] M.S. Kim, et al., Thin-film batteries for on-chip and wearable applications: advances, challenges, and future perspectives, Adv. Mater. 38 (2026) 7, https://doi.org/10.1002/adma.202515648.
[32] S. Dolabella, A. Borzì, A. Dommann, A. Neels, Lattice strain and defects analysis in nanostructured semiconductor materials and devices by high-resolution X-Ray diffraction: theoretical and practical aspects, Small Methods 6 (2022) 2, https://doi.org/10.1002/smtd.202100932.
[33] C. Wang, et al., Design of thin solid-state electrolyte films for safe and energy-dense batteries, Mater. Today 72 (2024) 235–254, https://doi.org/10.1016/j.mattod.2023.11.016.
[34] S. Guo, W. Kou, W. Wu, R. Lv, Z. Yang, J. Wang, Thin laminar inorganic solid electrolyte with high ionic conductance towards high-performance all-solid-state lithium battery, Chem. Eng. J. 427 (2022) 131948, https://doi.org/10.1016/j.cej.2021.131948.
[35] G. Vinay, R. Kant, A. Piiroinen, C. Nayak, A. Ganvir, H. Singh, Enhancing cold-sprayed nickel–aluminum bronze coatings on magnesium via scanner-based laser remelting, J. Therm. Spray Technol. (2026), https://doi.org/10.1007/s11666-025-02150-w.
[36] S. Behera, et al., Optimization of thin-film $Li_{1.0}Ni_{0.6}Co_{0.2}Mn_{0.2}O_2$ cathodes enabled by rapid thermal processing in oxygen-rich environments for superior lithium-ion battery performance, J. Mater. Chem. A Mater. 13 (35) (2025) 29196–29207, https://doi.org/10.1039/D5TA02870A.
[37] J.H. Kim, et al., Analogous design of a microlayered silicon oxide-based electrode to the general electrode structure for thin-film lithium-ion batteries, Adv. Mater. 36 (2024) 14, https://doi.org/10.1002/adma.202309183.

[38] R. Qiao, Y.-D. Chuang, S. Yan, W. Yang, Soft X-ray irradiation effects of $Li_2O_2$, $Li_2CO_3$ and $Li_2O$ revealed by absorption spectroscopy, PLoS One 7 (11) (2012) e49182, https://doi.org/10.1371/journal.pone.0049182.
[39] A. Sharafi, et al., Impact of air exposure and surface chemistry on Li–$Li_7La_3Zr_2O_{12}$ interfacial resistance, J. Mater. Chem. A Mater. 5 (26) (2017) 13475–13487, https://doi.org/10.1039/C7TA03162A.
[40] https://www.webqc.org/compound-Li7La3Zr2O12.
[41] E.A. Il'ina, A.A. Raskovalov, O.G. Reznitskikh, Thermodynamic properties of solid electrolyte $Li_7La_3Zr_2O_{12}$, J. Chem. Thermodyn. 128 (2019) 68–73, https://doi.org/10.1016/j.jct.2018.08.009.
[42] H. Mosqueda, H. Pfeiffer, Kinetic analysis of the thermal decomposition of $Li_4Ti_5O_{12}$ pellets, Process. Appl. Ceram. 5 (4) (2011) 199–203, https://doi.org/10.2298/PAC1104199M.
[43] W. Xia, et al., Reaction mechanisms of lithium garnet pellets in ambient air: the effect of humidity and $CO_2$, J. Am. Ceram. Soc. 100 (7) (2017) 2832–2839, https://doi.org/10.1111/jace.14865.
[44] M. Sahal, J. Guo, C.K. Chan, N. Rolston, Surface reduction of $Li_2CO_3$ on LLZTO solid-state electrolyte via scalable open-air plasma treatment, Batteries 10 (7) (2024) 249, https://doi.org/10.3390/batteries10070249.